

Intervening or associated? Machine learning classification of redshifted H I 21-cm absorption

S. J. Curran*

School of Chemical and Physical Sciences, Victoria University of Wellington, PO Box 600, Wellington 6140, New Zealand

Accepted —. Received —; in original form —

ABSTRACT

In a previous paper we presented the results of applying machine learning to classify whether an H I 21-cm absorption spectrum arises in a source intervening the sight-line to a more distant radio source or within the host of the radio source itself. This is usually determined from an optical spectrum giving the source redshift. However, not only will this be impractical for the large number of sources expected to be detected with the Square Kilometre Array, but bright optical sources are the most ultra-violet luminous at high redshift and so bias against the detection of cool, neutral gas. Adding another 44, mostly newly detected absorbers, to the previous sample of 92, we test four different machine learning algorithms, again using the line properties (width, depth and number of Gaussian fits) as features. Of these algorithms, three gave a some improvement over the previous sample, with a logistic regression model giving the best results. This suggests that the inclusion of further training data, as new absorbers are detected, will further increase the prediction accuracy above the current $\approx 80\%$. We use the logistic regression model to classify the $z_{\text{abs}} = 0.42$ absorption towards PKS 1657–298 and find this to be associated, which is consistent with a previous study which determined $z_{\text{em}} \approx 0.42$ from the K -band magnitude–redshift relation.

Key words: methods: data analysis – methods: statistical – radio lines: galaxies – quasars: absorption lines – galaxies: active – quasars individual: PKS 1657–298

1 INTRODUCTION

In absorption, the $\lambda = 21$ cm transition of neutral hydrogen (H I) traces the cool neutral gas in galaxies. Although the reservoir for all star formation, at redshifts of $z_{\text{abs}} \gtrsim 0.1$ (look-back times of $\gtrsim 1$ Gyr) there are only 142 H I 21-cm absorption systems currently known. Of these, 56 are due to a quiescent galaxy *intervening* the line-of-sight to a more distant radio continuum source and 82 are *associated* with the host of the radio source itself.

With its large instantaneous bandwidth, forthcoming surveys with the *Square Kilometre Array* (SKA) are expected to vastly increase the number of redshifted 21-cm absorption systems, which will give an unbiased census of the distribution and abundance of the star-forming reservoir over cosmic history. For example, observations of the Lyman- α transition in intervening systems show a flat redshift evolution of the cosmological mass density of H I (e.g. Crighton et al. 2017), which is at odds with the $z \sim 2$ peak in the star formation density (Hopkins & Beacom 2006; Behroozi et al. 2013). However, observations of 21-cm absorption suggest that the fraction of cold neutral gas exhibits a similar evolution as the star formation density (Curran 2019), thus providing a solution to the long-standing issue of the mismatch between the star-forming activity and the fuel supply.

Instantaneous coverage of the whole $z = 0 - 1$ redshift space is already possible with the *Australian Square Kilometre Array Pathfinder* (ASKAP, Allison et al. 2016), yielding several new detections (Allison et al. 2015, 2017, 2020; Moss et al. 2017; Sadler et al. 2020). Such spectral scanning is a powerful tool in detecting 21-cm absorption without the need for an optical spectrum, the requirement of which introduces a bias towards the most luminous and least dust-obscured sources, rendering the cool neutral gas undetectable (Curran et al. 2006; Curran et al. 2008). Whereas a detection of 21-cm absorption will yield a redshift, in the absence of an optical spectrum it is not known whether this is due to intervening or associated absorption. For example, it was unknown whether the $z_{\text{abs}} = 0.44$ H I 21-cm absorption detected towards PKS B1740–517 with ASKAP’s *Boolarly Engineering Test Array* was associated until Director’s Discretionary Time on *Gemini-South* confirmed optical emission lines at the same redshift (Allison et al. 2015).

Follow-up deep optical spectroscopy will be impractical for a large number of (optically faint) sources and impossible for those which do not exhibit spectral lines (blazars) or are optically undetected (e.g. Yan et al. 2012). One possible solution is the attainment of a photometric redshift via machine learning, specifically deep learning using neural networks. Training on optically selected samples (the *Sloan Digital Sky Survey*, SDSS), shows promising results with the validation giving accurate redshift predictions

* Stephen.Curran@vuw.ac.nz

for quasi-stellar objects (QSOs, Laurino et al. 2011; Brescia et al. 2013; D’Isanto & Polsterer 2018; Pasquet-Itam & Pasquet 2018; Beck et al. 2021). Training on SDSS QSOs can also provide a model which accurately predicts redshifts for radio selected sources (quasars, Curran et al. 2021). The model, however, requires measurements in nine photometric bands, spanning from the near-infrared to far-ultraviolet, which may not necessarily be available.

Thus, it would of great value to be able to confidently ascertain the nature of the 21-cm absorption without the need of an optical spectrum nor extensive multi-band photometry. Previously (Curran et al. 2016a), we used machine learning techniques, with the absorption line properties as features (see Table 1), to find that the absorber type could be predicted with $\approx 80\%$ accuracy. This is very promising for such a small training sample and so here we add a further 44, mostly new, systems to the 92 previously tested in order to further test the potential of this method.

2 ANALYSIS

2.1 The data

2.1.1 The sample

Previously (Curran et al. 2016a), the sample comprised 98 absorbers of which 53 were associated and 43 intervening. Checking the literature for detections published since and including absorbers which were missed, gives 136 in total of which 80 are associated and 56 are intervening (Table 1).¹ Note that during this process, we found duplicates and errors in the original data and, accounting for these, gives 48 associated and 44 intervening systems. As before, we include only absorption redshifts of $z_{\text{abs}} \geq 0.1$ in order to:

- Avoid resolved sight-lines, which will introduce a systematic difference between a low and high redshift sample.
- Minimise dilution of the absorption by 21-cm emission, which becomes an issue at $z \lesssim 0.1$ (e.g. Reeves et al. 2015).
- Maintain similar sample sizes between the two classes: If one sample is significantly larger than the other, the machine learning will simply favour the larger one based upon its higher probability of occurrence.

2.1.2 Extraction and processing of spectra

Since the spectra were generally unavailable, as before, we obtained these from the literature by digitising the appropriate figures. This was done using ADS’s *Dexter Data Extraction Applet* (Demleitner et al. 2001). Upon extraction, each spectrum was normalised by converting the ordinate to optical depth and the abscissa to velocity. In order to obtain the features required for the machine learning, Gaussians were fit to each spectrum using a custom written `pgplot` wrapper for the `python curve_fit` function, an example of which is shown in Fig. 1. Since all of the spectra had already had the continuum fitted or removed, we left this as is. The number of Gaussian profiles was obtained by minimising the χ -squared residual between the fit and the data where this led to a low number of profiles, otherwise the minimum number which gave a residual consistent with the noise from the line free part of the spectrum was

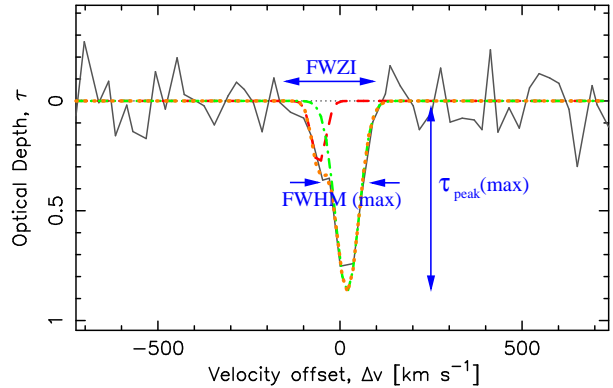


Figure 1. Example of Gaussian fits to a relatively noisy, but optically thick, absorption spectrum (Chowdhury et al. 2020). The ordinate has been normalised to optical depth and the abscissa to the velocity offset from the weighted mean value (see Curran et al. 2016a). The red and green fits show the individual Gaussian profiles and the orange fit the sum.

used. In most cases the number of profiles required was in agreement with the published number. As per Curran et al. (2016a), for the purpose of the FWZI, the end points of the profile were defined by where the compound fit reached an optical depth of $\tau < 10^{-4}$.

2.1.3 Features

We use the same features as previously, listed in Table 1 and shown in Fig. 1. These are the number of Gaussian fits to the profile, the span of the absorption and the width and depth information for the Gaussian components. As before, we also include the offset of the Gaussians from the weighted mean velocity over the whole spectrum, which is defined by the velocity which contains half of the velocity integrated optical depth.

The feature distributions are shown in Fig. 2. Apart from the redshift distributions, we see that the only real distinction is the velocity widths, with clear differences in the FWZIs and FWHMs. From the observed optical depths, Curran et al. (2016a) suggest that the additional nuclear component, hypothesised by unified schemes of active galactic nuclei (AGN, e.g. Antonucci 1993; Urry & Padovani 1995), could contribute to the broader associated profiles. The other/additional possibility is that associated absorption is preferably detected through the disk of the host (cf. Curran & Whiting 2010), whereas intervening absorption may be preferably detected in face-on systems, where the coverage of the background continuum is maximised (Curran et al. 2016b).

Interestingly, there is no difference in the number of Gaussian fits between the two classes. This was previously noted by Curran et al. and interpreted as being a consequence of the different noise levels in the spectra diluting intrinsic differences in the profiles. The associated absorbers also tend to be at lower redshift, due to the ionisation of the neutral gas by the active galactic nucleus in $z \gtrsim 1$ radio sources (Curran et al. 2019), although both classes are subject to an increasingly poor radio frequency environment as the observed frequency decreases from 1.4 GHz, making high redshift detection difficult.²

¹ There is an additional six $0.1 \lesssim z_{\text{abs}} \leq 0.21$ associated absorbers in Geréb et al. (2015), but since the spectra are unlabelled we cannot use these.

² Note also that the detection rate of intervening absorbers is also lower at $z_{\text{abs}} \gtrsim 1$ due to the geometry effects of an expanding Universe (Curran 2012).

Table 1. The features of the $z_{\text{abs}} \geq 0.1$ H I 21-cm absorbers not in the Curran et al. (2016a) sample. The first column gives the IAU name, followed by absorber type (associated/intervening), the absorption redshift, the number of Gaussian components fit to the profile, the Full-Width at Zero Intensity, the peak observed optical depths, the average offset of the components from the weighted mean velocity of the absorption, followed by this normalised by the FWZI and the Full-Width Half Maxima of the Gaussians. The last column gives the reference for the spectrum.

IAU	Type	z_{abs}	n_g	FWZI [km s ⁻¹]	τ_{peak}			$\overline{\Delta v}$ [km s ⁻¹]	$\overline{\Delta v}/\text{FWZI}$	FWHM			Ref.
					ave	max	min			ave	max	min	
B0003+380	A	0.229	2	59	0.032	0.053	0.011	-8.92	-0.15	19.5	30.7	8.3	A18
B0035+22	A	0.096	2	189	0.015	0.017	0.012	-5.0	-0.026	75.7	107	44.5	O17
J0146-0157	A	0.95904	3	1735	0.009	0.012	0.007	-25.5	-0.015	1019	1799	234	A19
B0202+14	A	0.8336	3	1155	0.13	0.022	0.004	-71.4	-0.061	194	416	83.0	J18
B0229+0044	A	1.2166	2	248	0.578	0.871	0.285	-19.4	-0.078	60.5	75.6	45.3	C20
B0229+0053	A	1.1630	2	365	0.327	0.478	0.177	34.6	0.095	84.4	94.9	73.8	C20
B0248+430	I	0.3939	3	52	0.160	0.191	0.117	0.57	0.011	5.35	6.31	4.75	L01
B0834-20	I	0.5906	3	78	0.090	0.107	0.080	-4.73	-0.060	17.3	31.4	4.08	S20
J0903+1622	A	0.1823	2	239	0.096	0.122	0.070	29.4	0.12	64.8	66.9	62.7	M17a
J0919+0146	I	1.27307	2	223	0.006	0.006	0.006	-10.7	-0.045	107	177	36.4	D17b
J0921+6215	I	1.10360	1	21.5	0.040	0.040	0.040	-0.37	-0.017	8.4	8.4	8.4	D17b
B0941-08	A	0.2281	3	380	0.0121	0.027	0.016	6.42	0.017	64.0	123	16.3	O17
J1013+2448	A	0.94959	3	412	0.005	0.006	0.004	59.2	0.14	98.6	316	31.7	A19
J1039+4612	A	0.1861	1	166	0.193	0.193	0.193	-8.77	-0.053	84.8	84.8	84.8	M17a
B1045+35A	A	0.84644	4	402	0.011	0.037	0.012	-8.21	-0.020	94.5	190	17.9	A19
B1147+557	A	0.13855	3	199	0.035	0.050	0.021	12.3	0.062	33.2	42.1	21.5	C11
B1200+045	A	1.226	2	188	0.015	0.022	0.009	4.4	0.023	36.6	49.4	23.7	A18a
J1206+6413	A	0.3710	2	189	0.006	0.011	0.002	42.0	0.22	87.6	90.5	84.6	V03
J1209-2032	A	0.4040	2	262	0.091	0.136	0.046	22.9	0.087	77.7	124	31.7	M20
B1221-423	A	0.171442	2	321	0.011	0.020	0.003	-33.7	-0.10	110	163	57	J10
B1245-197	A	1.2750	3	983	0.007	0.015	0.002	69.2	0.070	324	608	91	A18a
J1255+1817	I	0.75761	2	59	0.053	0.054	0.052	1.74	0.029	17.2	25.7	8.77	D17b
J1327+4326	I	0.95421	2	39	0.010	0.014	0.006	-5.90	-0.13	11.9	14.7	9.2	D17b
J1342+5110	I	1.48815	4	83	0.061	0.063	0.055	2.21	0.027	12.3	24.4	1.31	D17b
B1345+12	A	0.12174	2	249	0.006	0.010	0.002	27.3	0.11	95.8	121	71.0	G06
J1357+0046	A	0.797	2	330	0.016	0.017	0.015	18.7	0.057	79.9	99.1	60.7	Y16
J1428+2103	I	0.39401	2	27	0.171	0.220	0.122	0.12	0.004	6.69	9.67	3.71	D17a
B1456+375	A	0.33343	2	31	0.218	0.227	0.210	-1.50	-0.048	7.13	10.1	4.20	A18b
J1513+3431	A	0.1272	1	276	0.300	0.300	0.300	7.81	0.028	146	146	146	M17a
J1521+5508	A	1.0701	3	90	0.010	0.012	0.008	6.09	0.067	21.2	46.5	5.39	D19
J1534+2909	A	0.201	4	464	0.029	0.038	0.011	-12.4	-0.027	79.6	122	31.3	M17a
B1540-1453	A	2.1139	2	253	0.063	0.103	0.024	-9.63	-0.038	100	133	67.1	G21
B1549-79	A	0.15010	2	260	0.015	0.018	0.05	-8.4	-0.032	154	271	37.5	M01
J1551+0713	I	0.32891	1	12	0.097	0.097	0.097	-0.48	-0.04	3.97	3.97	3.97	D17a
B1555-140	A	0.0971	2	541	0.076	0.079	0.072	-14.1	-0.026	137	147	127	C06
J1602+5243	A	0.1057	2	207	0.007	0.010	0.004	-27.6	-0.13	53.56	58.0	49.1	C11
B1610-77	I	0.4503	3	87	0.027	0.037	0.022	2.82	0.032	18.5	30.0	5.9	S20
B1645+2230	A	0.82266	2	231	0.066	0.081	0.052	-3.59	-0.016	66.0	72.5	59.6	A19
B1657-298	-	0.42016	2	181	0.031	0.054	0.009	6.9	0.038	36.2	54.3	18.2	M17b
J1708+2111	A	0.2241	2	356	0.110	0.155	0.065	-38.4	-0.11	131	185	78	M17a
B1740-517	A	0.4413	3	211	0.072	0.173	0.008	16.9	0.080	17.3	58.0	10.7	A15
B1829-718	A	0.536	5	481	0.037	0.025	0.001	193	0.40	50.6	89	22	G19
B1954+513	A	1.2230	2	81	0.015	0.023	0.006	0.09	0.001	41.9	66.9	16.8	A17
J2219+0229	I	0.98075	2	43	0.139	0.188	0.090	-5.31	-0.12	9.85	10.32	9.85	D17b
J2245-3430	A	0.3562	1	39	0.128	0.128	0.128	1.18	0.031	13.7	13.7	13.7	A20
B2351+456	I	0.77945	1	118	0.228	0.228	0.228	-5.64	-0.048	60.3	60.3	60.3	D04

References: L01 – Lane & Briggs (2001), M01 – Morganti et al. (2001), V03 – Vermeulen et al. (2003), D04 – Darling et al. (2004), C06 – Curran et al. (2006), G06 – Gupta et al. (2006), J10 – Johnston et al. (2010), C11 – Chandola et al. (2011), A15 – Allison et al. (2015), Y16 – Yan et al. (2016), A17 – Aditya et al. (2017), D17a – Dutta et al. (2017a), D17b – Dutta et al. (2017b), M17a – Maccagni et al. (2017), M17b – Moss et al. (2017), O17 – Ostorero et al. (2017), A18a– Aditya & Kanekar (2018a), A18b – Aditya & Kanekar (2018b), J18 – Jones et al. (2018), A19 – Aditya (2019), D19 – Dutta et al. (2020), G19 – Glowacki et al. (2019), A20 – Allison et al. (2020), C20 – Chowdhury et al. (2020), M20 – Mhaskey et al. (2020), S20 – Sadler et al. (2020), G21 – Gupta et al. (2021).

Note: Moss et al. (2017) report a detection at $z_{\text{abs}} = 0.42016$, although, due to the lack of optical data, it is unknown whether this is associated or intervening.

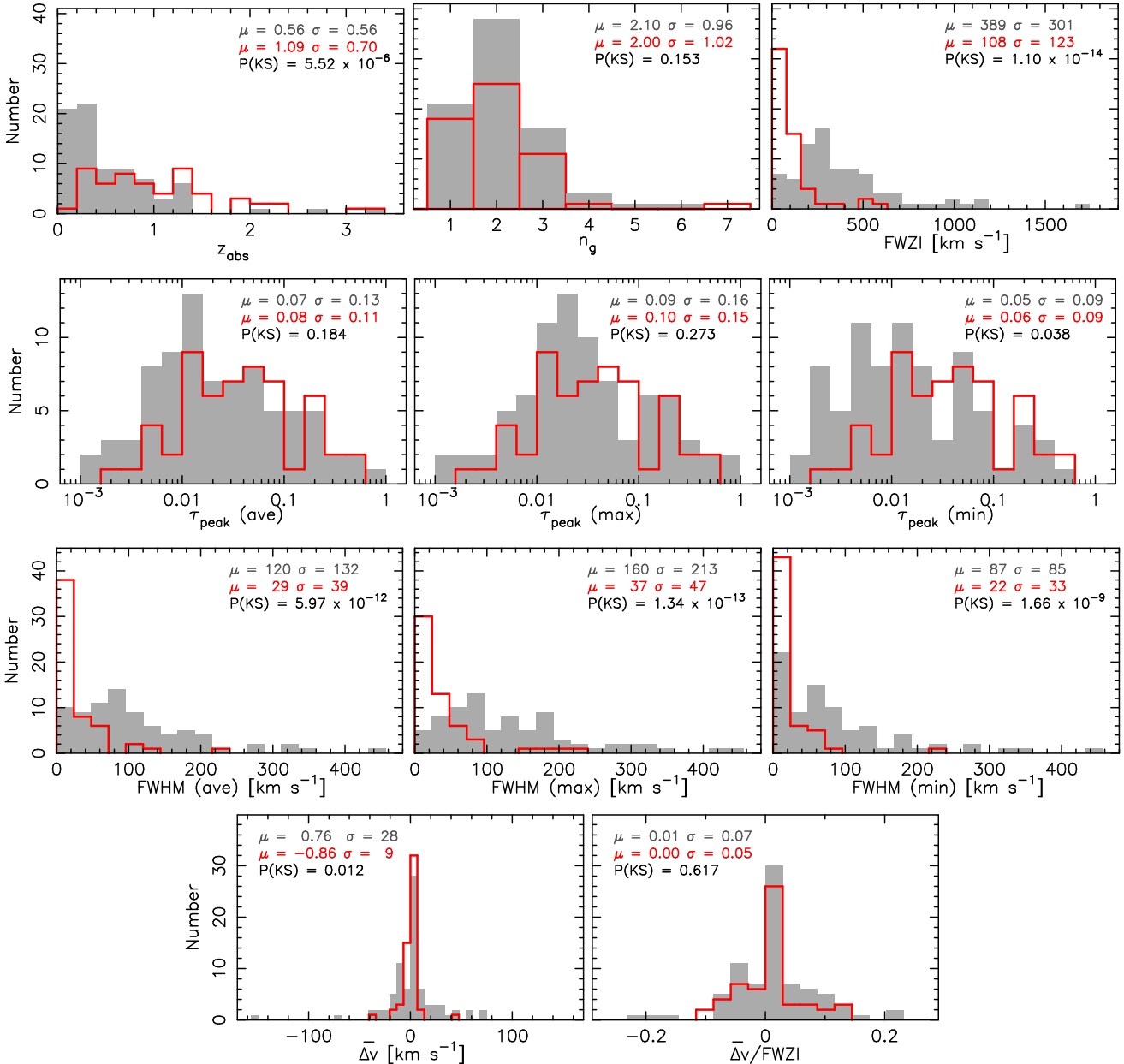


Figure 2. The distribution of features for the sample. The filled histogram represents the associated absorbers and the unfilled the intervening absorbers. In addition to the mean and standard deviation, we show the Kolmogorov-Smirnov probability that the associated and intervening absorbers are drawn from the same sample.

2.2 Machine Learning

In our previous study we used WEKA (Hall et al. 2009), a suite of machine learning algorithms, for the classification of the spectra. However, the `sklearn`³ module of python is more widely used by the astronomy community (e.g. Vanderplas et al. 2012) and can be run from the command line. This allows us to run a number of trials for each algorithm, shuffling the training and validation data each time in order to obtain a representative cross-validation score.

We test four types of common classifiers – *logistic regression*, *k-nearest neighbour*, *support vector classifier* and the *decision tree classifier*. Since there is a mismatch in the two binary classes (asso-

ciated & intervening), we perform random under-sampling, where 56 associated absorbers are randomly selected for training and validation. The data are then shuffled and the features normalised. Given the small size of the data-set, we use 10-fold cross-validation to split the data into ten sets, each of size $(56 + 56)/10 \approx 11$, of which ten are used to train the model and one to validate. This is repeated ten times, each time shuffling the data, with the mean accuracy being reported. This process is run 1000 times and the mean score of each algorithm recorded.

2.2.1 Logistic Regression

Logistic regression is analogous to multi-variable linear regression, but instead of a fit yields a binary result. Thus, it is particularly

³ <https://scikit-learn.org/stable/>

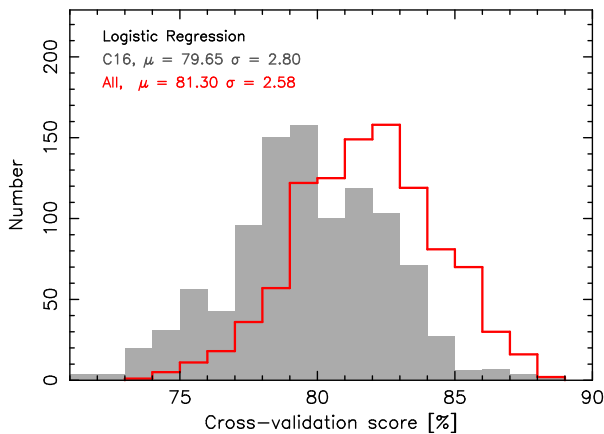


Figure 3. The results of 1000 trials using logistic regression, showing the mean score and standard deviation. The filled histogram represents the previous (Curran et al. 2016a) data and the unfilled histogram all of the data.

suit to this problem, where we are classifying an absorber as either associated or intervening. The algorithm compresses a linear combination of several variables (features) with a logistics sigmoid to yield a value of between 0 and 1. For the binary model, the prediction is labelled with one of these two end values, depending upon its probability ($0 \rightarrow 1$), or odds ($0 \rightarrow \infty$).⁴ For *even odds*, the values are 0.5 and 1, respectively. The algorithm has the advantage that is quicker than other machine learning techniques, although it is subject to the same errors as linear regression, such as skewing by outliers and the requirement of a sufficiently large sample. Also, the presence of a feature which perfectly separates the two binary classes will prevent the feature weight from converging, with the infinite optimal weight halting the training. Using the default `sklearn` values⁵, the logistic regression model of all of the data we get a mean cross-validation score of 81.3% (Fig. 3), which is a 1.7% ($\approx 0.6\sigma$) improvement over the previous data.

2.2.2 *k*-Nearest Neighbour

The *k*-nearest neighbour (kNN) algorithm maps the variables to a feature space and then compares the Euclidean distance between a test point and its *k* nearest neighbours. It then assigns a weighted combination of the target values with the nearest neighbours in order to place the test object in a group. The kNN algorithm is relatively computationally expensive and, like logistic regression, is sensitive to outliers. A further disadvantage is that irrelevant features can lead the learning astray. For the kNN method we are required to supply the number of neighbours to use and, from several mini-trials (of 10), we found that $k \approx 15$ was optimal, although anything in the range $k = 5 - 20$ gave similar results. The kNN algorithm has been used extensively in predictive modelling to obtain photometric redshifts from source magnitudes (e.g. Richards et al. 2001; Weinstein et al. 2004; Maddox et al. 2012; Han et al. 2016; Curran 2020). In this case we use it for binary classification, where it does not perform as well as the logistic regression. Furthermore, the additional data decreases the cross-validation score, resulting in a $\approx 1.2\sigma$ worse performance (Fig. 4).

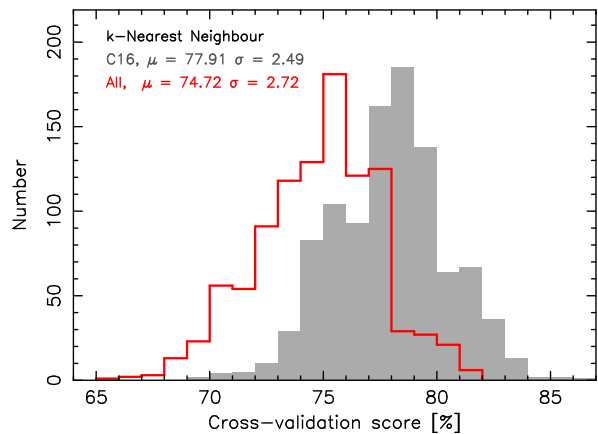


Figure 4. As Fig. 3, but for the *k*-nearest neighbour algorithm.

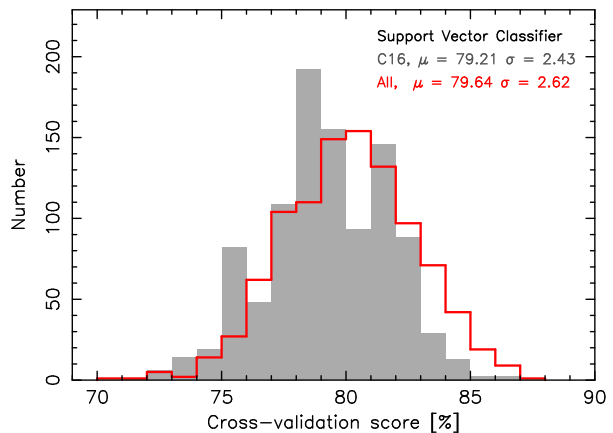


Figure 5. As Fig. 3, but for the support vector classifier.

2.2.3 Support Vector Classifier

A support vector machine constructs a hyperplane in a high dimensional space in order to perform classification, regression and outlier detection. Support vectors are points that reside closest to the hyperplane and in binary classification the training maximises the distance between the two categories. Further data are transformed into the same space and assigned a category based upon where in the space they are located. Although the support vector machine classifier (SVC) is computationally fast, it is not suitable for noisy data (overlapping features) nor large data sets. This could limit the applicability of this algorithm in classifying 21-cm absorption from large surveys (Sect. 1), although in this case the SVC is a reasonable performer. Using the default `sklearn` values⁶, we obtain a cross-validation score of $\approx 79\%$ for both the previous and the previous plus the additional data (Fig. 5).

2.2.4 Decision Tree Classifier

Like the other algorithms, decision trees can be used for both classification and regression. The algorithm builds a classification model based upon a tree structure, which branches the data-set (top node) into smaller subsets (child nodes), according to a predefined decision boundary. With one node on either side of the boundary,

⁴ We chose 0 for intervening and 1 for associated absorption.

⁵ https://scikit-learn.org/stable/modules/generated/sklearn.linear_model.LogisticRegression.html

⁶ <https://scikit-learn.org/stable/modules/generated/sklearn.svm.SVC.html>

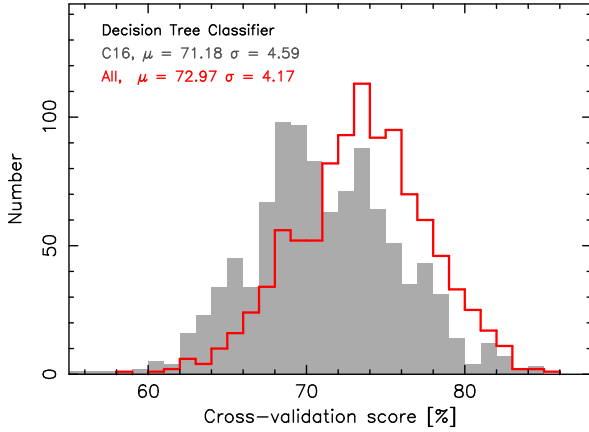


Figure 6. As Fig. 3, but for the decision tree classifier.

Table 2. The mean confusion matrix from 1000 runs of the logistic regression.

	Predicted associated		Predicted intervening	
	μ	σ	μ	σ
Actual associated	4.67	1.65	1.55	1.19
Actual intervening	1.27	1.12	6.52	1.78

the process is iterated through further branching until a predefined stopping criterion is reached. DTC has the advantage that it is not as sensitive to outliers as some of the other algorithms, although the tree choices can be biased due to the sequential nature of the algorithm. Over-fitting can also be a problem, which can be mitigated by limiting the maximum tree depth. From several mini-trials, we found the maximum depth to make little difference to the score and so used the default of no maximum depth, in which branches split until each “leaf” only contained a sample of two. From the 1000 trials, we see that the decision tree classifier (DTC) is the poorest performing algorithm (Fig. 6).

3 DISCUSSION

3.1 Results

We see that the logistic regression is best performer, giving a cross-validation score of $\gtrsim 80\%$, which improves with the addition of the new data. In Table 2 we show the mean confusion matrix of the test results obtained from 1000 runs of the logistic regression. That is, testing on data unseen by the algorithm gives a mean of 4.67 true positives (associated) and 6.52 true negatives (intervening), compared to 1.27 false positives and 1.55 false negatives. This gives a test score of $(4.67 + 6.52)/(4.67 + 6.52 + 1.27 + 1.55) = 0.80$, which is close to the cross-validation score.

The support vector classifier is the next best performer, with a mean score of $\approx 79\%$, which also improves with the addition of the new data. Following this is the k -nearest neighbour algorithm, but in this case the additional data significantly decreases the cross-validation score making this arguably the worst performer. Last, the decision tree classifier gives a mean score of $\approx 73\%$. Unlike the kNN, the DTC score increases with the new data, although the spread in values is wide ($\sigma \gtrsim 4\%$).

Table 3. The normalised importance of each feature for the k -nearest neighbour, support vector classifier and decision tree classifier. The means and standard deviations are obtained from 1000 trials of each.

Feature	kNN		SVC		DTC	
	μ	σ	μ	σ	μ	σ
z_{abs}	0	0.0005	0	0	0.198	0.045
n_g	0	0.001	0	0	0.009	0.013
FWZI	0.254	0.024	0.260	0.030	0.281	0.067
τ_{peak} (ave)	0	0	0	0	0.056	0.045
τ_{peak} (max)	0	0	0	0	0.057	0.051
τ_{peak} (min)	0	0	0	0	0.039	0.043
Δv	0	0.004	0	0.001	0.025	0.016
$\Delta v/\text{FWZI}$	0	0	0	0	0.046	0.043
FWHM (ave)	0.005	0.009	0.013	0.007	0.028	0.012
FWHM (max)	0.010	0.011	0.021	0.010	0.073	0.079
FWHM (min)	0.007	0.007	0.009	0.006	0.052	0.037

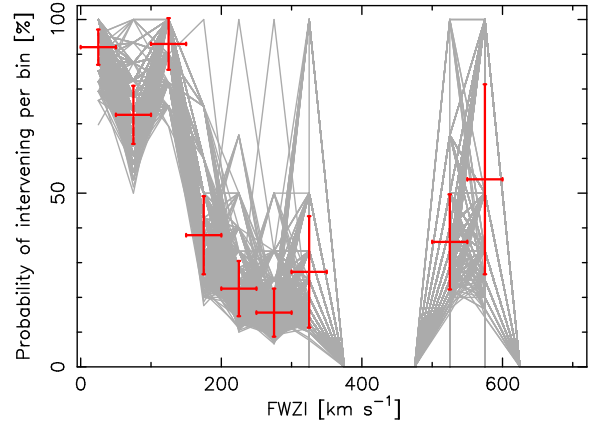


Figure 7. The probability of the absorber being intervening based upon the FWZI of the profile (cf. Fig. 2) in 50 km s^{-1} bins. The traces show each of the 1000 trials, where for each we randomly select 56 of the associated systems. The error bars show $\pm 1\sigma$ about the mean binned value.

3.2 Feature importance

Previously, we found the FWZI and FWHM to be the most important features and, while we can extract the coefficients of the logistic regression, these are given in terms of the odds ratio and are therefore not straightforward to interpret. We therefore show the feature importance for the other algorithms (Table 3), from which we see that the absorption redshift, number of Gaussian fits and the peak optical depth make zero contribution to the kNN and SVC algorithms and where these are non-zero, for the DTC algorithm, the values are often dominated by the scatter. While the FWHM makes a minor contribution, as noted by Curran et al. (2016a), the most important feature is the full line width.

This suggests the possibility of obtaining a probable absorber class from the FWZI alone. Fig. 7 shows the probability of the absorber being intervening for a given FWZI. From this, we see that if $\text{FWZI} \leq 50 \text{ km s}^{-1}$ there is a $\approx 90\%$ probability of the absorber being intervening, with even odds, on average, being reached between the $100 - 150 \text{ km s}^{-1}$ bins. Although subject to small numbers, this demonstrates that the type of absorption can only be predicted with $\gtrsim 70\%$ accuracy from the FWZI where this is $\lesssim 200 \text{ km s}^{-1}$.

In order to further quantify the contribution of the other features, in Fig. 8 we show the algorithm performances using only

the FWZI as a feature. From this, we see that the logistic regression exhibits the greatest improvement ($\approx 2\sigma$), with support vector classifier and decision tree classifier showing some to a lesser degree. Again, for the k -nearest neighbour algorithm the score decreases, although by a small amount with the binned modes being very close. This suggests that the LR algorithm makes most use of all the features and the kNN the least. The degradation in kNN score with the addition of the new data is therefore probably due to the introduction of noise from the other features as well as the new data not necessarily following a straightforward absorber type–FWZI relation: For the associated absorbers in the previous data $\overline{\text{FWZI}} = 416 \text{ km s}^{-1}$, cf. 389 km s^{-1} for all of the data. Since the new data moves the mean of the FWZI of the associated absorbers in the opposite sense to that expected, if basing the classification on the FWZI alone, we expect the algorithm to perform more poorly.⁷

3.3 The absorption towards PKS 1657–298

As stated in Table 1, because of the lack of an optical spectrum the nature of the $z_{\text{abs}} = 0.42016$ absorption towards PKS 1657–298 is unknown (Moss et al. 2017). We can, however, find the likely absorber type through a two-pronged approach: 1) prediction of the type from our logistic regression model and, 2) using machine learning to obtain the redshift of the background source. As described in Sect. 1, the latter can be obtained from a neural network trained on SDSS QSOs and then confidently applied to a radio selected source (Curran et al. 2021). The best results are obtained when the photometry from nine bands, spanning the far-ultraviolet to near-infrared ($FUV, NUV, u, g, r, i, z, W1, W2$), are used. Scraping the photometry from the *NASA/IPAC Extragalactic Database*, the *Wide-Field Infrared Survey Explorer*, the *Two Micron All Sky Survey* (Skrutskie et al. 2006) and *Galaxy Evolution Explorer* (Bianchi et al. 2017) databases, as described in Curran et al. (2021), we find the photometry to be limited to $\nu \leq 20 \text{ GHz}$ apart from one X-ray measurement. The lack of photometry, therefore, does not permit a photometric redshift determination.

Running 1000 trials to predict the absorber type from our logistic regression model, in 970 cases the absorption is classed as associated. Although, as mentioned above, there is no infrared photometry for PKS 1657–298, Moss et al. (2017) suggest that the measured $K = 14.9 \pm 0.1$ from 2MASS J17011004–2954423 may arise from PKS 1657–298, from which it is offset by 4.3". They then use the K -band magnitude–redshift relation (de Breuck et al. 2002; Willott et al. 2003) to obtain an emission redshift similar to that of the 21-cm absorption ($z_{\text{em}} \approx 0.42$), thus classifying the absorption as associated. However, this method of estimating the redshift is only effective for (radio) galaxies, providing, at best, a lower limit for quasar redshifts (Curran & Moss 2019). No AGN classification could be found for this object, although the observed X-ray flux of $4.9 \times 10^{-13} \text{ ergs cm}^{-2} \text{ s}^{-1}$, obtained from archival XMM-Newton data (Moss et al. 2017), gives a luminosity is $L_X \gtrsim 5 \times 10^{44} \text{ ergs s}^{-1}$ at $z \gtrsim 0.42$ (Fig. 9).⁸ This is relatively high (Georgakakis et al. 2015), in the range where the source

is likely to be a type-1 AGN (Heckman et al. 2005; Juneau et al. 2011; Singh et al. 2011). This is also in the range where star formation is believed to be suppressed by the AGN activity (Page et al. 2012, but see Curran & Duchesne 2019), thus suggesting that the source a quasar rather than a radio galaxy.

4 CONCLUSIONS

Being able to classify a redshifted H I 21-cm spectrum as intervening or associated without the need for an optical spectrum would provide a powerful diagnostic for detections with the next generation of large radio telescopes. Previously (Curran et al. 2016a), from a sample of 92 $z_{\text{abs}} > 0.1$ systems, of which 48 were associated and 44 were intervening, we found that machine learning algorithms could predict the absorber type with an $\approx 80\%$ accuracy. Updating the sample with the addition of 44 absorption systems not previously included, we run four separate classifiers 1000 times in order to obtain a typical cross-validation score. We find that three of these give a slight improvement in the score over the previous sample, with the fourth worsening. In decreasing order of score:

- Logistic regression gives a mean score of 81.3%, compared to 79.7% for the previous sample.
- Support vector classification gives a mean score of 79.6%, compared to 79.2%.
- k -Nearest neighbour gives a mean score of 74.2%, compared to 79.9%.
- Decision tree classification gives a mean score of 73.0%, compared to 71.2%.

For all algorithms we find the line-widths to be the most important features, particularly the full-width at zero intensity, although, except for the kNN, this on its own does not perform as well as the full feature complement. This is most pronounced for the highest scoring algorithm (LR), while for the kNN algorithm, which exhibits a decrease in accuracy upon the addition of the new data, the inclusion of the other features makes little difference to using the FWZI alone. The presence of “irrelevant features” leading the learning astray is a known issue with k -nearest neighbour. We therefore believe that the kNN is assigning most of the weighting to the FWZI and, given that the mean FWZI of the associated absorbers in the whole sample is lower than the previous sample, this leads to a poorer performance.

We use the logistic regression model to classify the $z_{\text{abs}} = 0.42$ absorption towards PKS 1657–298 which, in the absence of an optical spectrum, is unknown (Moss et al. 2017). Out of 1000 trials, the absorption is flagged as associated in 970 cases, which is consistent with Moss et al., who, from the K -band magnitude–redshift correlation for galaxies, estimate a source redshift of $z_{\text{em}} \approx z_{\text{abs}}$. However, this assumes the K -band magnitude of a near-by source and the X-ray luminosity of $L_X \gtrsim 5 \times 10^{44} \text{ ergs s}^{-1}$ suggests that the continuum source is a type-1 object (quasar), for which the K -band magnitude–redshift relation does not hold (Curran & Moss 2019). Thus, although, we also find the absorption to be associated, there is some uncertainty in the Moss et al. classification.

With this increase in sample size, giving what are still very limited numbers, logistic regression appears to be the best performer and also the algorithm which makes most use of all of the spectral features. This is also the case, to a lesser extent, for the support vector classification. The decision tree classifier also improves with the addition of the new data, but with a mean score

⁷ For the intervening absorbers, $\overline{\text{FWZI}} = 118 \text{ km s}^{-1}$ for the previous data, cf. 108 km s^{-1} for all of the data.

⁸ NED lists a 2–10 keV flux of $7.68 \times 10^{-13} \text{ ergs cm}^{-2} \text{ s}^{-1}$, which is due to a Galactic low-mass X-ray binary (Verbunt 2001; Verrecchia et al. 2007).

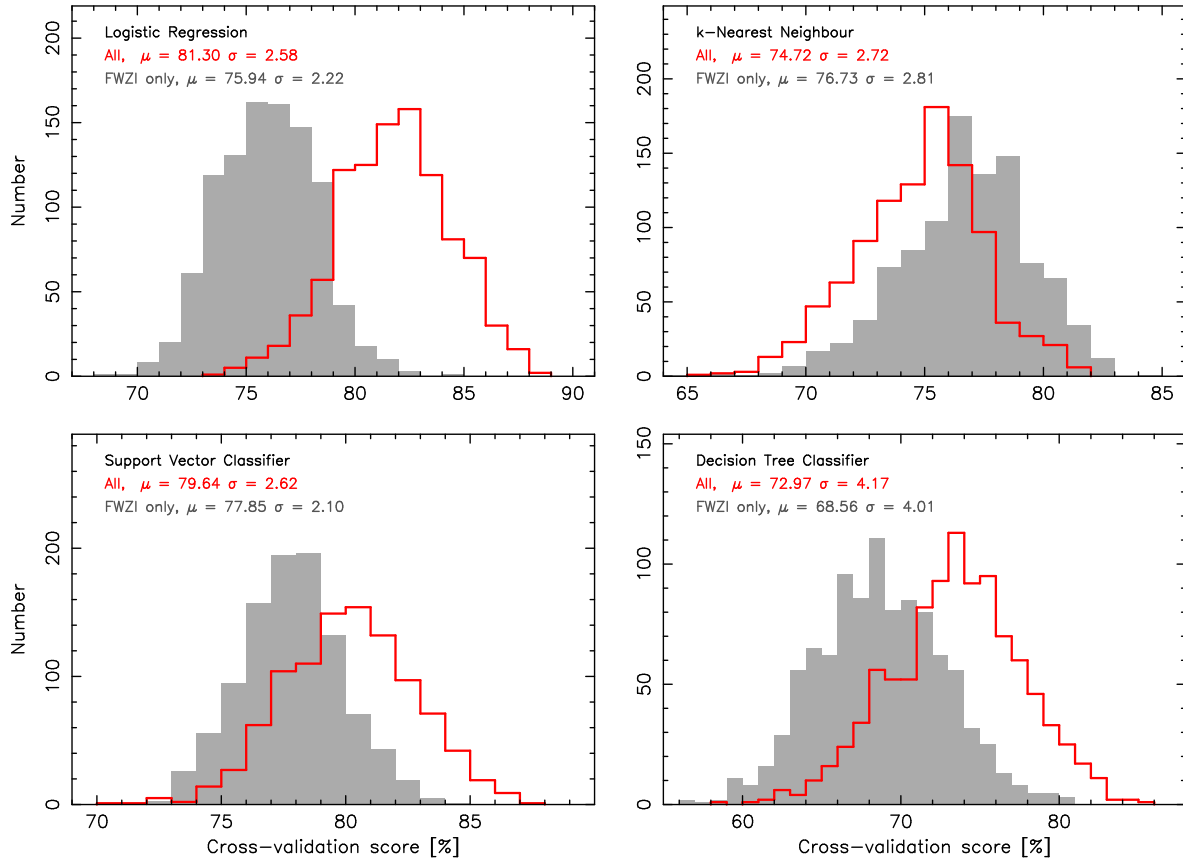


Figure 8. Comparison between machine learning with all features (unfilled histogram) and FWZI only (filled histogram) over 1000 trials.

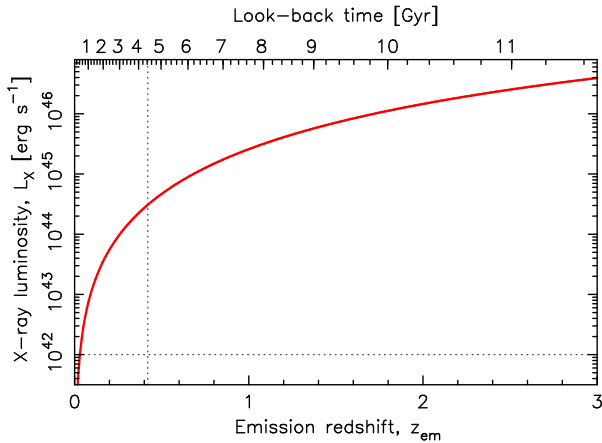


Figure 9. The X-ray luminosity of PKS 1657–298 as a function of redshift. The dotted vertical line designates the absorption redshift and the horizontal line designates the lower limit for an AGN (Page et al. 2012).

of 73% this falls short of the LR and SVC performance ($\approx 80\%$). Although more accurate at $\approx 75\%$, the kNN algorithm appears to be basing its predictions on the FWZI alone, which results in a degradation of score with the addition of the new data. Based upon this small sample, it appears higher accuracies maybe be achievable with the logistic regression algorithm trained upon appropriately sized samples. With the addition of more training data over the next few years, this could provide an important diagnostic for forthcoming surveys with the Square Kilometre Array.

ACKNOWLEDGEMENTS

I wish to thank the referee, Jeremy Darling, for his very helpful comments. This research has made use of the NASA/IPAC Extragalactic Database (NED) which is operated by the Jet Propulsion Laboratory, California Institute of Technology, under contract with the National Aeronautics and Space Administration and NASA's Astrophysics Data System Bibliographic Service. This research has also made use of NASA's Astrophysics Data System Bibliographic Service.

DATA AVAILABILITY

The data underlying this article are available in its online supplementary material.

REFERENCES

- Aditya J. N. H. S., 2019, MNRAS, 482, 5597
- Aditya J. N. H. S., Kanekar N., 2018a, MNRAS, 473, 59
- Aditya J. N. H. S., Kanekar N., 2018b, MNRAS, 481, 1578
- Aditya J. N. H. S., Kanekar N., Prochaska J. X., Day B., Lynam P., Cruz J., 2017, MNRAS, 465, 5011
- Allison J. R. et al., 2017, MNRAS, 465, 4450
- Allison J. R. et al., 2020, MNRAS, 494, 3627
- Allison J. R. et al., 2016, Astronomische Nachrichten, 337, 175
- Allison J. R. et al., 2015, MNRAS, 453, 1249
- Antonucci R. R. J., 1993, ARA&A, 31, 473

- Beck R., Szapudi I., Flewelling H., Holmberg C., Magnier E., 2021, *MNRAS*, 500, 1633
- Behroozi P. S., Wechsler R. H., Conroy C., 2013, *ApJ*, 770, 57
- Bianchi L., Shiao B., Thilker D., 2017, *ApJS*, 230, 24
- Brescia M., Cavuoti S., D’Abrusco R., Longo G., Mercurio A., 2013, *ApJ*, 772, 140
- Chandola Y., Sirothia S. K., Saikia D. J., 2011, *MNRAS*, 418, 1787
- Chowdhury A., Kanekar N., Chengalur J. N., 2020, *ApJ*, 900, L30
- Crighton N. H. M. et al., 2017, in *IAU Symposium*, Vol. 321, Formation and Evolution of Galaxy Outskirts, Gil de Paz A., Knapen J. H., Lee J. C., eds., pp. 309–314
- Curran S. J., 2012, *ApJ*, 748, L18
- Curran S. J., 2019, *MNRAS*, 484, 3911
- Curran S. J., 2020, *MNRAS*, 493, L70
- Curran S. J., Duchesne S. W., 2019, *A&A*, 627, A93
- Curran S. J., Duchesne S. W., Divoli A., Allison J. R., 2016a, *MNRAS*, 462, 4197
- Curran S. J., Hunstead R. W., Johnston H. M., Whiting M. T., Sadler E. M., Allison J. R., Athreya R., 2019, *MNRAS*, 484, 1182
- Curran S. J., Moss J. P., 2019, *A&A*, 629, A56
- Curran S. J., Moss J. P., Perrott Y. C., 2021, *MNRAS*, 503, 2639
- Curran S. J., Reeves S. N., Allison J. R., Sadler E. M., 2016b, *MNRAS*, 459, 4136
- Curran S. J., Whiting M. T., 2010, *ApJ*, 712, 303
- Curran S. J., Whiting M. T., Murphy M. T., Webb J. K., Longmore S. N., Pihlström Y. M., Athreya R., Blake C., 2006, *MNRAS*, 371, 431
- Curran S. J., Whiting M. T., Wiklind T., Webb J. K., Murphy M. T., Purcell C. R., 2008, *MNRAS*, 391, 765
- Darling J., Giovanelli R., Haynes M. P., Bower G. C., Bolatto A. D., 2004, *ApJ*, 613, L101
- de Breuck C., van Breugel W., Stanford S. A., Röttgering H., Miley G., Stern D., 2002, *AJ*, 123, 637
- Demleitner M., Accomazzi A., Eichhorn G., Grant C. S., Kurtz M. J., Murray S. S., 2001, in *Astronomical Society of the Pacific Conference Series*, Vol. 238, Astronomical Data Analysis Software and Systems X, Harnden F. R. J., Primini F. A., Payne H. E., eds., p. 321
- D’Isanto A., Polsterer K. L., 2018, *A&A*, 609, 111
- Dutta R., Raghunathan S., Gupta N., Joshi R., 2020, *MNRAS*, 491, 838
- Dutta R., Srianand R., Gupta N., Joshi R., 2017a, *MNRAS*, 468, 1029
- Dutta R., Srianand R., Gupta N., Joshi R., Petitjean P., Noterdaeme P., Ge J., Krogager J.-K., 2017b, *MNRAS*, 465, 4249
- Georgakakis A. et al., 2015, *MNRAS*, 453, 1946
- Geréb K., Maccagni F. M., Morganti R., Oosterloo T. A., 2015, *A&A*, 575, 44
- Głowacki M. et al., 2019, *MNRAS*, 489, 4926
- Gupta N., Salter C. J., Saikia D. J., Ghosh T., Jeyakumar S., 2006, *MNRAS*, 373, 972
- Gupta N. et al., 2021, *ApJ*, submitted (arXiv:2103.09437)
- Hall M., Frank E., Holmes G., Pfahringer B., Reutemann P., Witten I., 2009, *SIGKDD Explorations*, 11, 10
- Han B., Ding H.-P., Zhang Y.-X., Zhao Y.-H., 2016, *Research in Astronomy and Astrophysics*, 16, 74
- Heckman T. M., Ptak A., Hornschemeier A., Kauffmann G., 2005, *ApJ*, 634, 161
- Hopkins A. M., Beacom J. F., 2006, *ApJ*, 651, 142
- Johnston H. M., Broderick J. W., Cotter G., Morganti R., Hunstead R. W., 2010, *MNRAS*, 407, 721
- Jones K. M., Ghosh T., Salter C. J., 2018, *AJ*, 155, 254
- Juneau S., Dickinson M., Alexander D. M., Salim S., 2011, *ApJ*, 736, 104
- Lane W. M., Briggs F. H., 2001, *ApJ*, 561, L27
- Laurino O., D’Abrusco R., Longo G., Riccio G., 2011, *MNRAS*, 418, 2165
- Maccagni F. M., Morganti R., Oosterloo T. A., Geréb K., Maddox N., 2017, *A&A*, 604, A43
- Maddox N., Hewett P. C., Péroux C., Nestor D. B., Wisotzki L., 2012, *MNRAS*, 424, 2876
- Mhaskey M., Paul S., Gupta N., Mukherjee D., Gopal-Krishna, 2020, *A&A*, 643, A174
- Morganti R., Oosterloo T. A., Tadhunter C. N., van Moorsel G., Killeen N., Wills K. A., 2001, *MNRAS*, 323, 331
- Moss V. A. et al., 2017, *MNRAS*, 471, 2952
- Ostorero L., Morganti R., Diaferio A., Siemiginowska A., Stawarz Ł., Moderski R., Labiano A., 2017, *ApJ*, 849, 34
- Page M. J. et al., 2012, *Nature*, 485, 213
- Pasquet-Itam J., Pasquet J., 2018, *A&A*, 611, A97
- Reeves S. N., Sadler E. M., Allison J. R., Koribalski B. S., Curran S. J., Pracy M. B., 2015, *MNRAS*, 450, 926
- Richards G. T. et al., 2001, *AJ*, 122, 1151
- Sadler E. M. et al., 2020, *MNRAS*, 499, 4293
- Singh V., Shastri P., Risaliti G., 2011, *A&A*, 532, A84
- Skrutskie M. F. et al., 2006, *AJ*, 131, 1163
- Urry C. M., Padovani P., 1995, *PASP*, 107, 803
- Vanderplas J., Connolly A., Ivezić Ž., Gray A., 2012, in *Conference on Intelligent Data Understanding (CIDU)*, pp. 47–54
- Verbunt F., 2001, *A&A*, 368, 137
- Vermeulen R. C. et al., 2003, *A&A*, 404, 861
- Verrecchia F., in’t Zand J. J. M., Giommi P., Santolamazza P., Granata S., Schuurmans J. J., Antonelli L. A., 2007, *A&A*, 472, 705
- Weinstein M. A. et al., 2004, *ApJS*, 155, 243
- Willott C. J., Rawlings S., Jarvis M. J., Blundell K. M., 2003, *MNRAS*, 339, 173
- Yan T., Stocke J. T., Darling J., Hearty F., 2012, *AJ*, 144, 124
- Yan T., Stocke J. T., Darling J., Momjian E., Sharma S., Kanekar N., 2016, *AJ*, 151, 74